5th International Conference on Multiphase Flow, ICMF'04
Yokohama, Japan, May 30–June 4, 2004
Paper No. 122

Experiments and Computations on Drop Impact at a Liquid/Liquid Interface

Zulfaa Mohamed-Kassim[1], Ellen K. Longmire[2], Jun-Seok Kim[3], Xiaoming Zheng[3], John Lowengrub [3]

1: School of Aerospace Engineering, Science University of Malaysia, Malaysia, zulfaa@eng.usm.my
2: Dept. of Aerospace Engineering & Mechanics, University of Minnesota, USA, ellen@aem.umn.edu
3: Department of Mathematics, University of California, Irvine, CA, USA, lowengrb@math.uci.edu

Abstract The evolution of single droplets impacting on liquid/liquid interfaces was investigated experimentally using flow visualization and PIV. A water/glycerin solution was used for the drop and the ambient fluid beneath the interface, and silicone oil was used for the less dense ambient. Two viscosity ratios (drop to ambient fluid), λ, of 0.14 and 0.33 were studied. The corresponding Reynolds numbers based on the drop diameter, impact velocity, and ambient viscosity were 20 and 68. Upon impact, the drop deformed the interface significantly before rebounding upward and eventually settling to a 'rest' position on top of a thin film. The vorticity initially present within the drop dissipated fairly rapidly due to drop/interface interaction as well as shearing of the trailing wake on the upper drop surface. Equivalent axisymmetric and two-dimensional flows were simulated numerically using interface capturing phase-field and level-set methods respectively that we have recently developed. In the two-dimensional case, an adaptive unstructured mesh is used to better capture the near contact dynamics. The non-adaptive axisymmetric simulations agree well with the experiments up to the times at which the drop and interface come into near contact. At this point, the non-adaptive simulations prematurely predict coalescence. The adaptive simulation shows significant improvement over the non-adaptive simulations due to its ability to better resolve the thinning of fluid between the bounding interfaces before coalescence occurs.

1. Introduction

The present work is motivated by the desire to understand and model the coalescence process. In general, coalescence occurs when a force drives two bodies toward each other. The two bodies could be separate droplets or one droplet and a larger fluid volume with a nominally flat interface. When the bodies collide, they typically deform, and a thin film of liquid remains between them. This film must escape or drain away before the bodies can merge. When the film gap decreases to a submicroscopic scale (~0.01 μm), van der Waals forces can cause the neighboring interfaces to merge so that the bodies coalesce. Coalescence between separate fluid volumes occurs in many industrial and environmental applications, and the rate of coalescence (or non-coalescence) is a key parameter in determining process efficiency or environmental outcome. It is therefore desirable to be able to predict and simulate such rates numerically.

Accurate numerical simulations face several challenges however. First, the simulation must employ either an interface tracking or capturing method that progresses stably through the coalescence transition. Second, the simulation requires a method of resolving larger scales on the order of a drop diameter (~ cm) as well as very small scales associated with the thin film. In the current study, we consider a flow where gravity drives a drop of one liquid through a surrounding of a second liquid until it impacts on and interacts with a horizontal interface lying above the drop's homophase. During the drop impact, the underlying interface deforms and then rebounds until the drop eventually reaches a macroscopic 'rest' position. A microscopic thin film continues to separate the drop and the underlying interface long after the macroscopic motion associated with the initial momentum and vorticity of the falling drop dissipates. The film drainage that eventually leads to coalescence is essentially decoupled from the original impact. Because of the range of

scales as well as the decoupling between impact and coalescence, this flow is very challenging to simulate numerically.

The current study has two parallel goals. First, we attempt to quantify drop impact dynamics experimentally by performing real-time visualization and planar particle image velocimetry (PIV) measurements. Second, we attempt to develop a viable numerical method to simulate this flow accurately. In the following sections, we describe the experimental and numerical methods. Then, we describe the behavior observed experimentally and compare the results to numerical simulations. Finally, in the last section, we present conclusions.

2. Experimental Set Up and Methods

A transparent glass tank of 40 cm square cross section and 30 cm height was filled with a 10 cm layer of silicone oil on top of a 13 cm layer of water/glycerin mixture (~45% glycerin by volume). Two types of silicone oil, Dow Corning 200® Fluid with viscosities of 20 cs and 50 cs, were used. Drops that fell through the silicone oil were composed of the same water/glycerin mixture. The indices of refraction of the liquids were matched as closely as possible to minimize optical distortions in the photographic imaging. Both the drop and the lower liquid layer were dyed with a very small amount of Rhodamine 6G to make them visible against the silicone oil. For PIV measurements, the bulk liquids and the drops were seeded with titanium dioxide tracer particles of ~2 μm diameter.

Drops were released from a glass tube positioned near the top of the Dow Corning fluid layer using an electronically-triggered valve. Each drop reached a terminal velocity, U_i, before impacting the liquid/liquid interface below. The characteristic parameters for the two fluid combinations are given in Table 1. The Reynolds number (Re) is defined as $\rho_s U_i D/\mu_s$, and the Weber number is defined as $\rho_d U_i^2 D/\sigma$. The subscripts d and s represent the drop liquid and the surrounding silicone oil, respectively.

Table 1. Experimental parameters.

	Units	Dow Corning 200® Fluid 20 cs	Dow Corning 200® Fluid 50 cs
Diameter, D	cm	1.03	1.03
Drop impact velocity, U_i	cm/s	13.2	9.8
Drop impact time scale, t_i	ms	78	105
Gravity time scale, tg	ms	78	80
Density ratio, ρ_d/ρ_s		1.189	1.178
Viscosity ratio, $\lambda = \mu_d/\mu_s$		0.33	0.14
Reynolds number, Re		68	20
Weber number, We		7.0	3.8
Froude, Fr		1.0	0.6

PIV experiments were performed in vertical planes intersecting the drop cross-section. A high-frequency camera system (NAC Memrecam c.i.) captured flow sequences illuminated by vertical light sheets from a Quantronix 527 DQE-S Nd:YLF laser pulsed at 500 Hz. At this frame rate, the camera resolution was 572 x 432 pixels. Sequences were captured for two fields of view: 3.0 cm x 2.3 cm and 1.5 cm x 1.2 cm. To avoid image distortion caused by small mismatches in refractive indices, the camera was inclined upward at an angle of ~12º to view through the interface from below. To avoid laser light refraction by the meniscus at the glass/liquid interface intersection, the laser sheet was also inclined upward through the interface.

To obtain local velocity vectors, consecutive images were interrogated with a cross-correlation routine using *PIV Sleuth* software (Christensen and Soloff, 2000). The time difference between

consecutive images was 2 ms. For the lower magnification experiments, interrogation areas were 32 x 32 pixels with 50% overlap. For the higher magnification experiments, initial vectors were obtained using interrogation areas of 64 x 64 pixels with 75% overlap. Then, the image was re-interrogated using smaller areas of 32 x 32 pixels with 50% overlap. The second interrogation was computed iteratively based on the initial vectors. The total uncertainty in the resulting velocity vectors was $0.02U_i$ and $0.01U_i$ for the low and high magnification experiments, respectively. Uncertainty in Gaussian peak-fitting was the dominant contributor. Spatial velocity gradients and vorticity were computed based on a three-point central-difference method.

To view three-dimensional effects associated with the drop coalescence, additional visualizations were performed using a relatively thick (~ 2 cm) laser sheet aligned horizontally and coincident with the liquid/liquid interface. Tracer particles in the bulk liquids were allowed to settle out so that only the liquid/liquid interface was marked. The camera viewed the interface through a mirror located inside the tank and inclined at 45^o to the horizontal. In this case, the camera and the laser were synchronized to operate at 100 Hz. More details on the experimental facility and measurement techniques can be found in Mohamed-Kassim and Longmire (2003).

3. Numerical Methods and Implementation

Numerical simulations of drop/interface impact were performed using interface-capturing phase-field (Kim, Kang, Lowengrub 2004) and level-set methods (Zheng, Cristini, Lowengrub, Anderson 2004) we have recently developed. In the former, a concentration field c is introduced, interfaces have a finite thickness, and the concentration field is coupled (consistent with thermodynamics) to the Navier-Stokes equations through the bulk fluid properties (*e.g.* density, viscosity) and singular reactive stresses that depend on concentration gradients and mimic surface tension, *i.e.* in the Boussinesq approximation, the nondimensional equation is

$$\frac{\partial \mathbf{u}}{\partial t} + \mathbf{u}\cdot\nabla\mathbf{u} = -\nabla p - \frac{\varepsilon}{We}\nabla\cdot\left(\nabla c\nabla c\right) + \frac{1}{\mathrm{Re}}\nabla\cdot\left(\mu(c)\mathbf{D}\right) - \frac{1}{Fr}\rho(c)\hat{z}\,,$$

where $\mathbf{D} = \nabla\mathbf{u} + \nabla\mathbf{u}^T$ is the deformation tensor and ε is proportional to the interface thickness. The concentration field satisfies a nonlinear, fourth order advection-diffusion equation in which the diffusion is limited to occur only near interfaces separating the flow components, *i.e.*

$$\begin{aligned} &\frac{\partial c}{\partial t} + \mathbf{u}\cdot\nabla c = \frac{1}{Pe}\nabla\cdot\left(m(c)\nabla\eta\right), \\ &\eta = f'(c) - \varepsilon^2\nabla^2 c \end{aligned}$$

where $m(c)$ is the mobility, Pe is the diffusional Peclet number, η is the chemical potential and $f(c)$ is the double-welled free energy. Thus sharp interfaces are replaced by narrow transition layers. Once a layer from one interface interacts with a layer from another, a topological change smoothly occurs driven by diffusion. This mimics the effect of van der Waals forces. A drawback of this approach is that typically 4-5 grid points are needed to resolve the transition layer (and accurately calculate the reactive stresses). Thus when a uniform mesh of linear size h is used, the computational interface thickness is $\approx 6\varepsilon$, when the standard fourth order polynomial $f(c) = c^2\left(1-c\right)^2/4$ is used for the free energy, so that the resulting $\varepsilon \approx 2/3\,h$ is much larger than the true interface thickness. Further, classical hydrodynamics is only obtained at length scales $l \gg \varepsilon$ (Lowengrub and Truskinovsky, 1998). In coalescence problems, for example, this means

that hydrodynamic lubrication forces will only accurately calculated at gap-widths $w \gg \varepsilon$. The fact that this lower bound depends on the grid size h is a fundamental difficulty that arises in all interface capturing methods.

Significant improvement in performance can be made if the grid is made adaptive such that the grid size h_Σ near an interface Σ is much smaller than a uniform grid size h used in smooth regions of the flow. Accordingly, we have recently developed adaptive remeshing techniques for 2D and 3D domains using unstructured triangular and tetrahedral meshes (Zheng, Cristini, Lowengrub, Anderson 2004). These techniques can be applied to any interface capturing method, including the phase-field approach described above. As a first test of the usefulness of the adaptive remeshing, however, we have applied the remeshing to a finite element implementation of the level-set method. In this approach, the interfaces are identified as the zero set of a function (level-set function), and the singular surface tension stresses $\kappa \mathbf{n} \delta_\Sigma$ (where κ is the curvature, $\mathbf{n}$ is the interface normal and δ_Σ is the surface delta function) are spread to a narrow region on the volume mesh surrounding the interface. The thickness of this region is proportional to the grid size h. The heaviside function evaluated as a function of the level-set function is an approximation of the concentration field described above.

The mesh refinement algorithm is based on minimizing a mesh energy functional using local restructuring operations (*e.g.* equilibration, node addition/subtraction, edge-swapping). The mesh energy density ρ_N scales as $(l_{loc})^{-3}$ where l_{loc} is a measure of the local length scales to be resolved (*i.e.* distance from the interface, interface curvature, gap-width). The accuracy is set by two parameters l_{loc} and s_{loc} where s_{loc} is the rate of mesh coarsening away from the interface. The number of mesh points needed to resolve the local length scales is therefore minimized.

The phase-field system is solved using a second order accurate finite difference projection method using efficient multigrid methods we have recently introduced (Kim, Kang, Lowengrub 2004). In the level-set method, the flow equations are solved using a Crank-Nicolson time discretization together with a standard P^2-P^1 finite element method in space. In the mesh adaption we use here, the local length scale is taken to be proportional to the distance to the interface.

4. Results

4.1 Experiments

In the PIV experiments, the drop to ambient viscosity ratio λ is the key parameter differentiating the two liquid combinations used. The two cases will be referred to hereafter using either their viscosity ratio or Reynolds number. A characteristic time scale based on the impact velocity is defined as $t_i = D/U_i$ and another characteristic time scale based on gravity is defined as:

$$t_g = \sqrt{\frac{D}{(\Delta\rho/\langle\rho\rangle)g}}, \tag{2}$$

where $<\rho>$ is the average density between the two liquids. A Froude number which measures the ratio of gravity to inertial forces can be defined as $(t_g/t_i)^2$. As can be seen in Table 1, the effects of gravity and inertial forces are in fact comparable for both cases (for the lower λ value, viscous drag decreases the inertia compared to the gravity effect).

In figures 1a-d (λ = 0.14) and 1e-f (λ = 0.33), outlines of the drop fluid boundary and the interface extracted from the low magnification experiments are shown sequentially. From these

boundary profiles, normalized centerline locations of the lower drop surface, upper drop surface, and the underlying interface are obtained and plotted in figures 2a and 2b. The impact time ($t = 0$) is defined as the time the lower drop surface crosses the quiescent interface level. In all results, length and time are scaled with D and t_i, respectively.

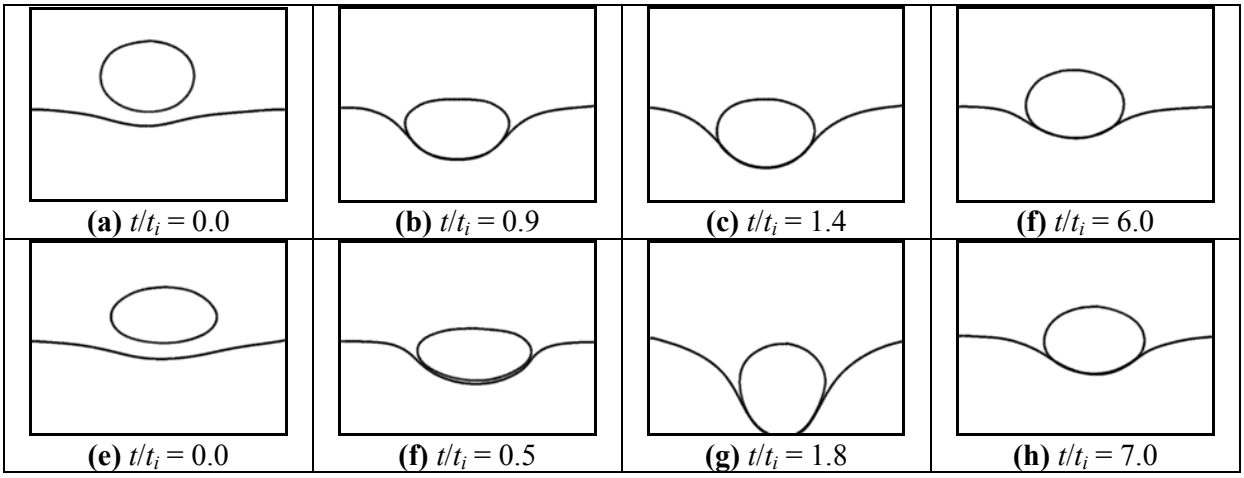

Figure 1. Time evolution of the drop for $\lambda = 0.14$ (a, b, c, d) and for $\lambda = 0.33$ (e, f, g, h).

In a separate publication (Mohamed-Kassim and Longmire, 2003), it was shown that both drops have reached terminal velocity and steady spheroidal shapes before impact. Due to its higher *Re* and *We*, the drop in the lower viscosity surrounding is more oblate (see figures 1a and 1e). At the time of impact, higher capillary pressure inside the spheroidal drops allows them to maintain their steady shape while the interfaces have deformed (figures 1a and 1b). The interfaces start to deflect downward about $1.0t_i$ before impact. As each drop nears the interface, a radial pressure gradient builds up underneath the drop which begins to drain the trapped ambient fluid outward. The drop then stretches horizontally as it 'touches' the interface. Figures 1b and 1f show both drops stretching to a maximum; the deformation is more pronounced when *Re* and *We* are larger. With time, the remaining inertia inside the drop deflects the interface to a maximum while the drop extends vertically at the same time (figures 1c and 1h). When $\lambda = 0.14$, the interface deflects to a maximum of $0.64D$ beneath the quiescent interface level at $1.4t_i$. For $\lambda = 0.33$, this deflection is $1.1D$ at $1.8t_i$. In general, the degree of deformation depends strongly on the viscosity ratio.

From figures 2a and 2b, both the drops and the interface continue to deform until they reach a steady state approximately $6t_i$ and $7t_i$; after impact. When $\lambda = 0.14$, the planar interface and the drop center undergo one complete oscillation before the translational motion is dissipated. Interestingly, when the ambient viscosity is smaller, the upper drop surface oscillates locally while the interface beneath it reaches its maximum deflection. Finally, the shapes of both drops and the interface at rest appear identical (see figures 2d and 2h) because the state of any stationary fluid is not affected by viscosity. In our experiments, the drops are seen to rest on the interface for about 30 seconds when $\lambda = 0.33$ and 60 seconds when $\lambda = 0.14$. In both cases, coalescence is inhibited by a thin film of ambient fluid trapped between the drop and the interface. Direct analysis of the flow images shows that the thin film thickness is of order 400 μm when the macroscopic 'steady state' condition is achieved. The coalescence time can increase up to four times if the ambient liquid is void of any seed particles.

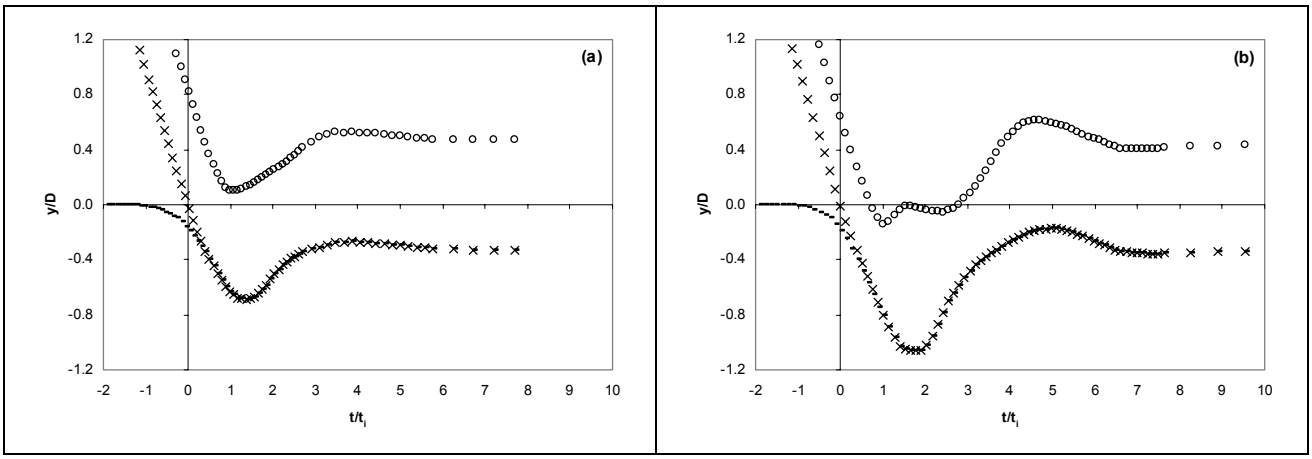

Figure 2. Normalized locations of interface (-), lower drop surface (x), and upper drop surface (o) on the centerline relative to quiescent interface through the impact for λ=0.14 (a) and λ=0.33 (b).

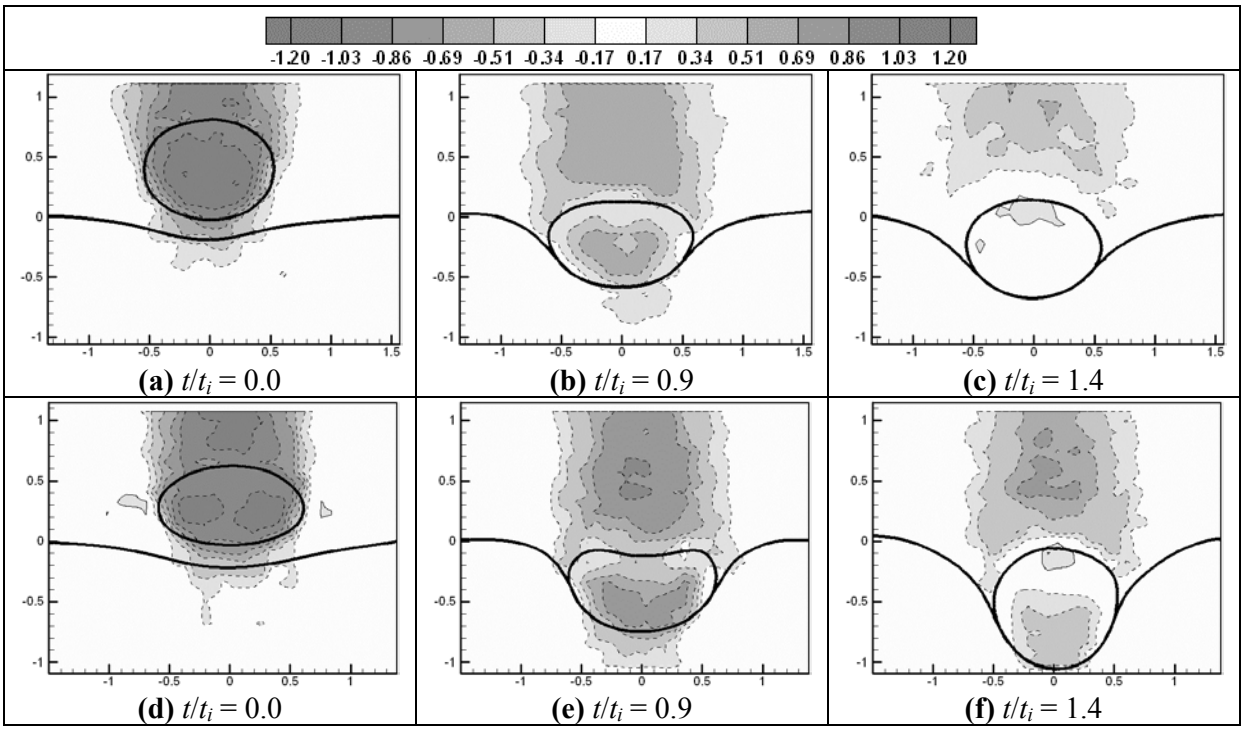

Figure 3. Normalized vertical velocity contour plots for λ = 0.14 (a, b, c) and for λ = 0.33 (d, e, f). Positive values (upward velocities) are shown with solid lines and negative values with dashed lines.

Additional visualization experiments carried out on drops in the ranges $0.3 < Re < 300$ and $0.005 < We < 8.4$ showed rebounding behavior similar to that described above, i.e. the drops did not coalesce immediately after impact. Instead, the rest period, corresponding with the film drainage period preceding coalescence, typically lasted a long time. For the PIV cases described, this time was ~50 times longer than the time required to dissipate the original drop circulation.

Figures 3a-c (λ = 0.14) and 3d-f (λ =0.33) show contour plots of the normalized vertical velocity field, v/U_i, extracted from the PIV analysis of the low magnification images. To study the same flow evolution in more detail especially inside the drop, normalized vorticity fields from high magnification images are shown in figures 4a-f. The corresponding normalized absolute velocity vector fields are shown in figures 5a-f.

Prior to impact, each drop generates a wake in the ambient liquid upstream. In the higher λ case, a region within the wake moves faster than the drop itself, suggesting that the ambient fluid is rotating around a vortex ring within the wake (see figure 3d). Another rotational zone exists inside each drop as evident from the vorticity contour plots at the time of impact (see figures 4a and 4d). In these plots, the positive and negative vorticity values near the drop right and left edges, respectively, represent a vortex ring inside the drop. This internal fluid rotation is induced by viscous shear stresses at the drop boundary. The maximum vorticity value at the core of this vortex ring is approximately $9U_i/D$ for the lower λ case and $18U_i/D$ for the higher λ case (the levels shown extend only to magnitudes of 8). At the time of impact, the interface at the centerline is moving downward at a rate of about $0.3U_i$ in both cases (see figures 3a and 3d). Meanwhile, the ambient fluid beneath the drop appears to be pushed radially outward (see figures 6a and 6d).

When the drop touches the interface at $0.9t_i$, the inertia of the drop as well as the wake dissipates due to the resistive interfacial tension force (see figures 3b and 3e). However, in the higher *Re* case, the wake inertia is still large enough to cause a local indentation in the upper drop surface. Competing effects of the wake inertia and the capillary force cause the upper drop surface to oscillate locally as observed in figure 2b. At the same time, vorticity values inside the drop are also reduced to $7U_i/D$ and $10U_i/D$ for λ = 0.14 and 0.33, respectively. The impinging wake, which carries another vortex ring inside it, shears the upper drop surface and thus generates a counter-rotating ring that straddles the upper drop surface (figure 4b and 4e). The wake shearing in effect dissipates the fluid rotation about the main ring inside the drop. The wake shearing near the upper drop surface can be observed in the vector plots in figures 5b and 5e. Other causes of vorticity dissipation inside the drop are interfacial resistance and drop deformation (for more details see Mohamed-Kassim and Longmire 2003).

At $1.4t_i$, the interface reaches its maximum deflection for λ = 0.14. Meanwhile, the maximum velocity inside the wake has decreased to approximately $0.5U_i$ while the fluid within the drop and the ambient fluid near the drop are nearly immobile (see figure 3c). On the other hand, for λ = 0.33, the wake inertia is larger with a maximum velocity of $0.8U_i$ (figure 3f). Comparing these two cases, the drop shape is more prolate for higher *Re* (higher λ). From the vorticity contour plots (figures 4c and 4f), it is clear that the maximum vorticity value inside each drop near the main ring has reduced significantly. At this time, the wake continues to impinge on and shear the upper drop surface causing the counter-rotating ring that straddles the upper drop surface (see figures 5c and 5f).

When the interface rebounds, the upward surface tension force and the downward wake inertia stretch both drops to a maximum horizontal width. During this time, an opposing (but weak) vortex ring is generated inside each drop due to the combined effect of the wake shearing on the surface and the interfacial rebound. The vorticity inside each drop completely dissipates when the drop comes to a rest position (see figure 2).

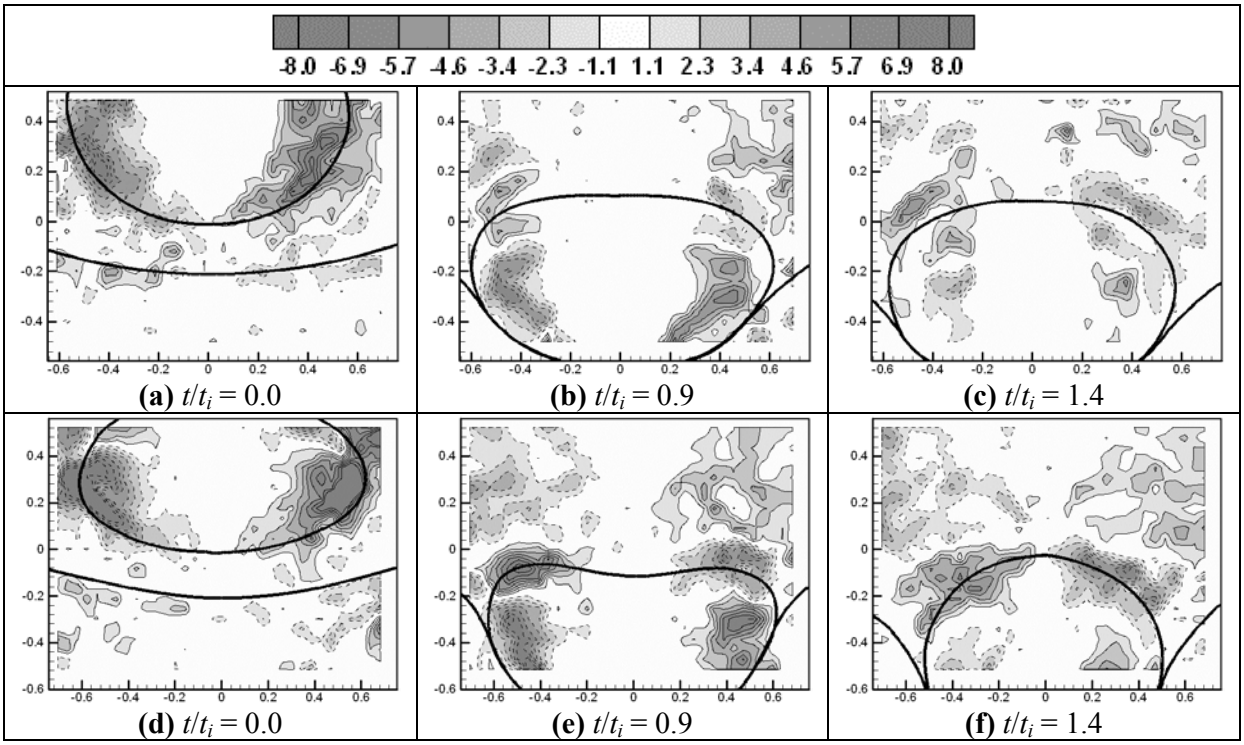

Figure 4. Normalized vorticity contour plots for $\lambda = 0.14$ (a, b, c) and for $\lambda = 0.33$ (d, e, f). Positive values (counterclockwise rotation) are shown with solid lines and negative values with dashed lines.

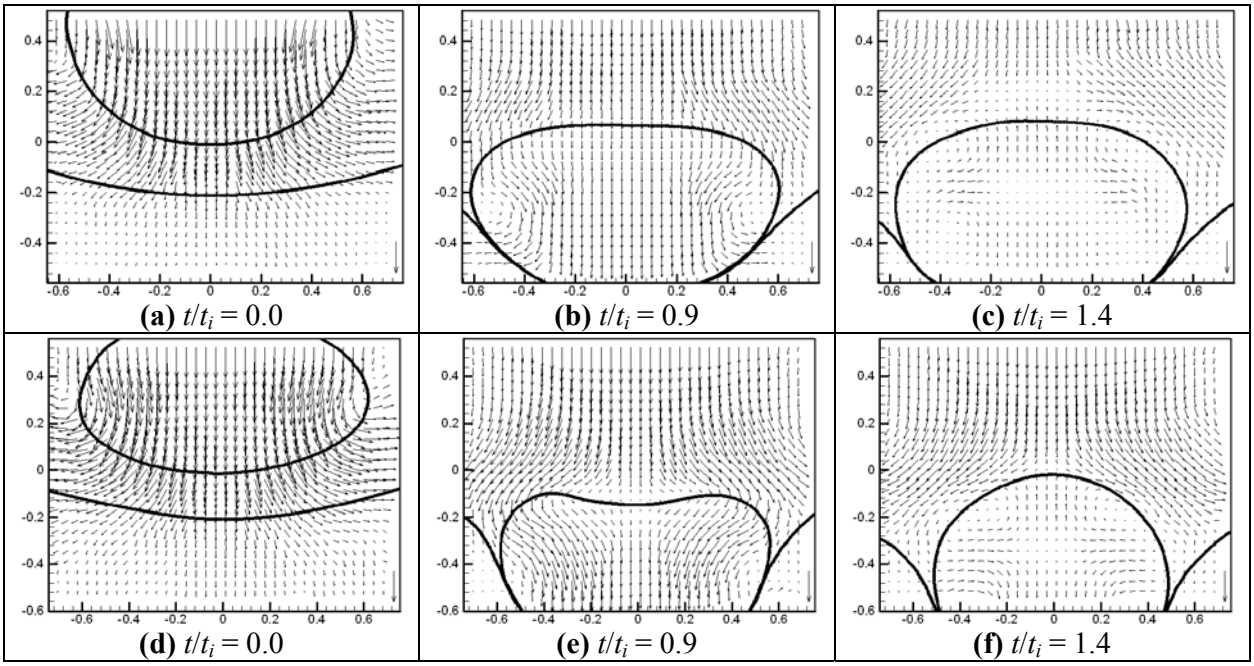

Figure 5. Time evolution of the absolute velocity vector fields for (a, b, c) and for $\lambda = 0.33$ (d, e, f). A reference vector of magnitude $1.0U_i$ is placed at the bottom right corner of each image.

4.2 Simulations

We performed simulations using the phase-field and level-set methods to simulate the experimental conditions. All physical parameters are matched from the experiment. Due to computational costs, the initially spherical drops were placed approximately 3D above the flat interface. That is, the lower drop surface is at a distance 3D from the flat interface. The initial velocity is taken to be the incompressible projection of $-U_i$ in the drop interior and zero in the matrix ambient. In the case of the lower viscosity ratio $\lambda = 0.14$, the drop appears to reach a steady shape before impacting the interface. In the case when $\lambda = 0.33$, the drop seems to be still evolving at impact. In the phase-field simulations, the interface thickness parameter $\varepsilon = .005$, the Peclet number $Pe = 1/\varepsilon$ and the mobility $m(c) = c(1-c)$. Results from the axisymmetric phase-field model are presented in figures 6-8. In the adaptive mesh simulations, results are presented for l_{loc}=0.007 and s_{loc}=0.6. The adaptive two-dimensional simulation results are shown in figures 9 and 10.

In figure 6, a comparison of the numerical (thick) and experimental (thin) drop/interface morphologies at time t/t_i=0 are shown for the two cases $\lambda = 0.14$ (a) and $\lambda = 0.33$ (b). The non-adaptive, axisymmetric phase-field method is used with interface thickness . In the former case, the agreement between the simulations and experiments is excellent. In the latter case $\lambda = 0.33$, the numerical drop and interface are more deformed than that from the experiment. Further, the distance between the numerical lower drop surface and the interface is slightly smaller than that for the experiment. We believe these deviations are due to the fact that the numerical drop is still evolving and has not yet reached a steady-shape unlike the experiment where the drop has reached a steady shape prior to impact. This is partly confirmed by preliminary tests where even larger deviations between simulations and experiments occurred when the initial drop/interface gap is smaller (2D).

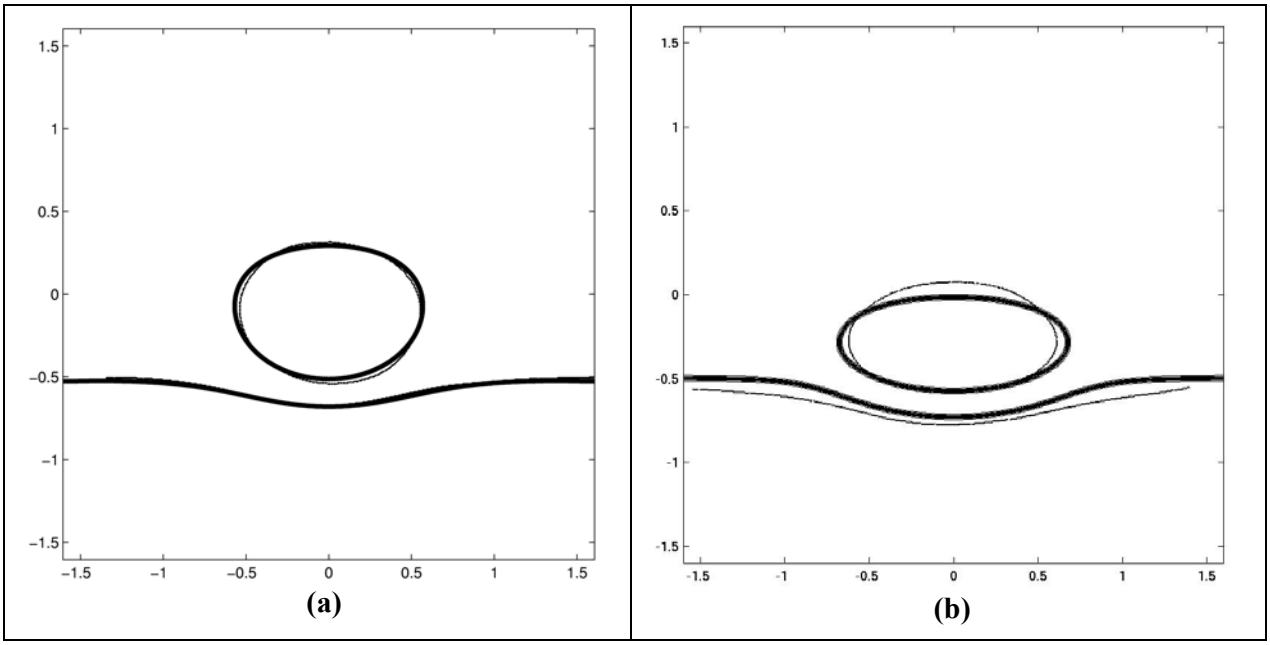

Figure 6. A comparison of the experimental (thin) and numerical (thick) results at t/t_i=0 for $\lambda = 0.14$ (a) and for $\lambda = 0.33$ (b) using the phase-field (non-adaptive) method.

In figure 7, the drop morphologies and vorticity contours are shown for $\lambda = 0.14$ (a-c) and $\lambda = 0.33$ (d-f). The contour levels match the values used in the experiments shown in figure 4. The features are very similar to those obtained in the experiments. As in the experiments, there is a vortex ring inside the drop induced by the viscous shear stresses at the interface. As in the experiment, the core is located near the regions of high drop curvature. The values of vorticity at the core are very close

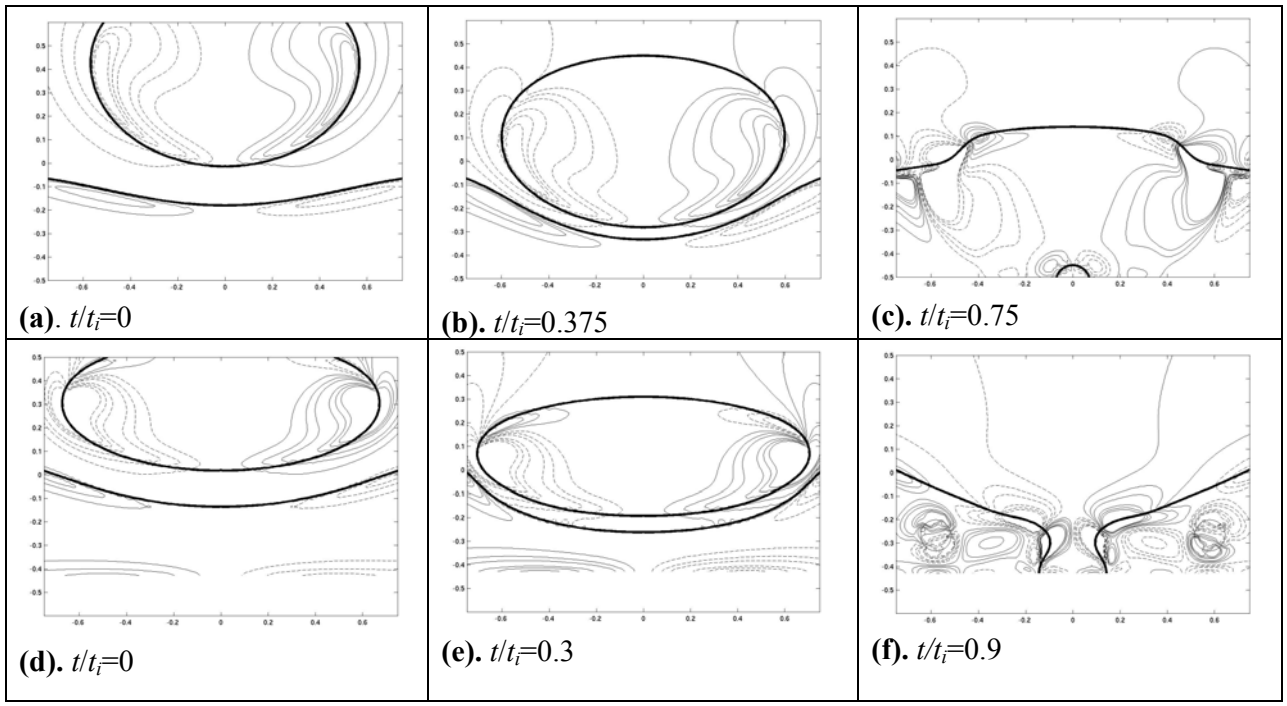

Figure 7. Normalized vorticity contour plots from the phase-field simulations for $\lambda = 0.14$ (a, b, c) and for $\lambda = 0.33$ (d, e, f). The contour levels match those from the experiments (shown in figure 4).

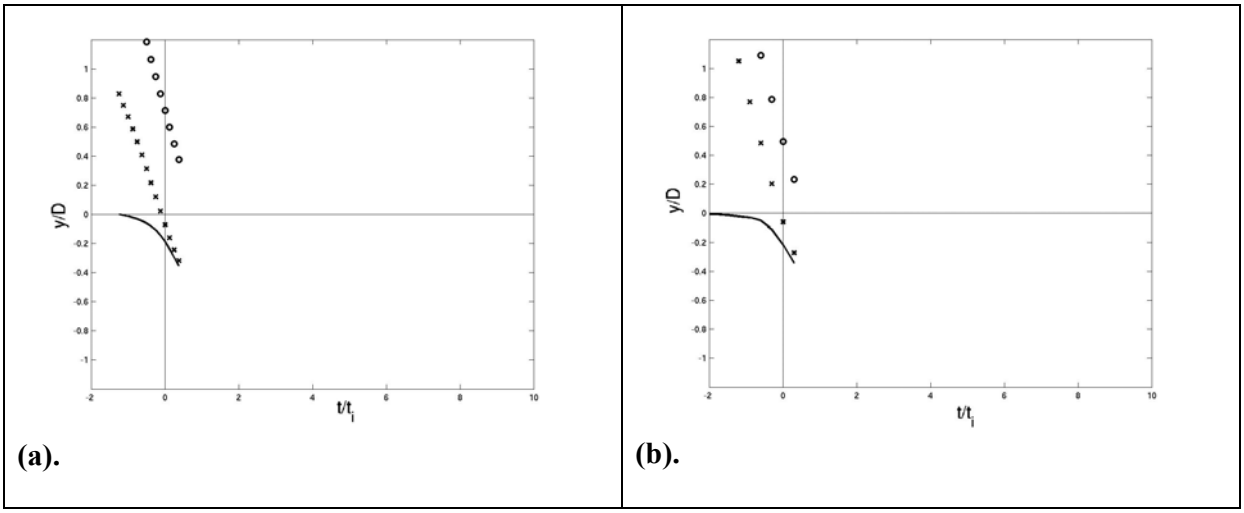

Figure 8. Normalized locations of interface (-), lower drop surface (x), and upper drop surface (o) on the centerline relative to quiescent interface through the impact for λ=0.14 (a) and λ=0.33 (b). Results from the phase-field simulations. Coalescence occurs after the last times shown.

to those obtained in the experiment when $\lambda = 0.14$. The vorticity is larger than that of the experiment when $\lambda = 0.33$ (i.e. 19 U_i/D). Further, when $\lambda = 0.33$, the vortex ring extends further into the matrix fluid. Indeed, taking viscosity-matched fluids, the vortex ring would be centered at the interface and thus would equally extend into the drop and matrix fluids.

In contrast to the experiments, however, we see that the drop coalesces with the lower fluid upon impacting the interface. This is shown more clearly in figure 8 where the normalized locations of the numerical upper and lower drop surfaces and interface are shown for the two cases as a function of time. In the phase-field simulations, when the lower drop surface comes within ε (*e.g.* 7 mesh points) of the interface, coalescence occurs. Prior to impact, the approach is nearly linear in time and the results are very similar to those obtained from the experiments. Although the rate of approach of the numerical drop when $\lambda = 0.14$ appears to be slightly slower than in the experiment, we believe this is due to our particular initial condition.

Together, the results in figures 6-8 strongly suggest that the phase-field method is quantitatively accurate until the drop comes into near contact with the interface. At these resolutions, the non-adaptive method is not able to resolve the lubrication forces in the near contact region however.

The adaptive simulation shows significant improvement over the non-adaptive simulations in resolving the near contact region. Since the method is applied in two-dimensions, we make only qualitative comparisons with the experiments and the axisymmetric phase-field simulations. The development of axisymmetric adaptive methods is a subject of future work. In figure 9, the drop and interface positions are shown together with the adaptive mesh for the two sets of experimental parameters $\lambda = 0.14$ (a-c) and $\lambda = 0.33$ (d-f). As in the experiments and the axisymmetric phase-field simulations, the drop and interface in the latter case are more deformed. The adaptive mesh is highly refined near the drop surface and interface and rapidly coarsens away from it. Further, observe that both mesh refinement and coarsening occurs dynamically to keep the mesh bound to the surfaces and interface. When $\lambda = 0.14$, the onset of coalescence is seen at t/t_i=1.0. Coalescence occurs as asymmetrically with rupture beginning at the left hand side of the drop. The asymmetry occurs because the mesh is not symmetric. Interestingly, this asymmetry mimics the real situation in which asymmetric rupture is observed in recent experiments on drop/interface coalescence (Mohamed-Kassim and Longmire 2004).

One of the difficulties with level-set methods is that the mass (of flow components) is not conserved by the algorithm. This is evident here particularly in $\lambda = 0.33$ where the drop and interface are quite deformed. We are currently testing techniques to correct for the mass loss. For example, one promising technique seems to be the use of a coupled level-set/volume-of-fluid (CLSVOF) approach where the volume fraction function is used to reset the level-set function to exactly conserve component masses. We have recently developed an adaptive two-dimensional CLSVOF method for Stokes flows and performed highly resolved simulations of drops in extensional flow (Yang, James, Lowengrub, Zheng and Cristini 2004). The application of this method to the Navier-Stokes equations is the subject of future work.

To demonstrate the effectiveness of the mesh in capturing the lubrication forces in the near contact region between the drop and interface, in figure 10, we present the distance between the lower drop surface and interface as a function of time for the simulations shown in figure 9 together with results using a less refined mesh (l_{loc}=0.01). Here the time shown is not shifted by the impact time. Observe that the coalescence time is delayed by increasing the local resolution. This is particularly evident in the $\lambda = 0.33$ case.

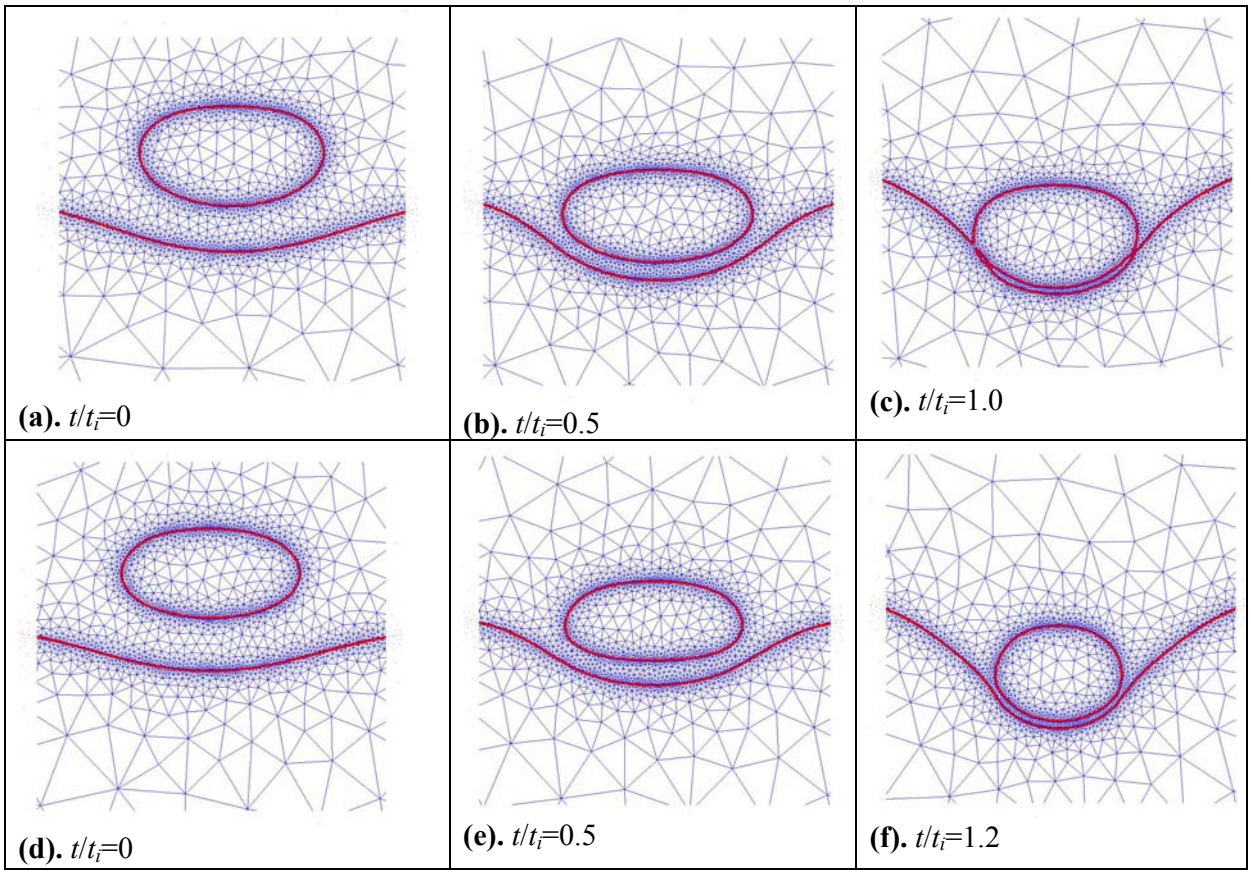

Figure 9. The interface profiles and adaptive mesh from the two-dimensional adaptive level-set method for $\lambda = 0.14$ (a, b, c) and for $\lambda = 0.33$ (d, e, f).

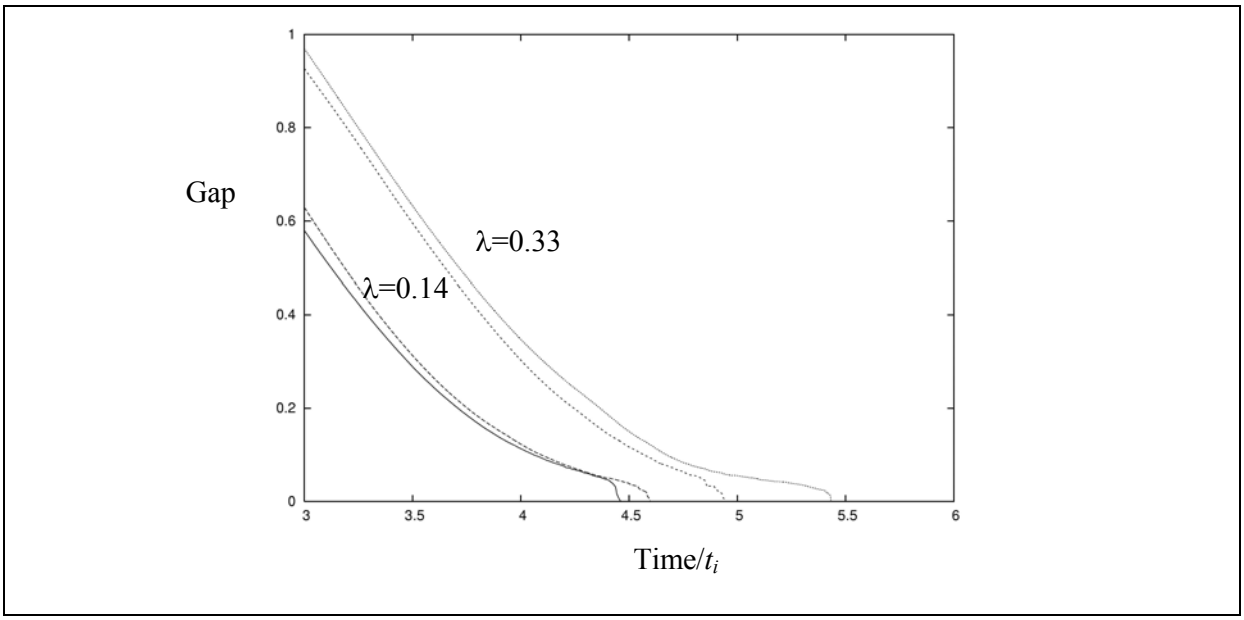

Figure 10. The distance between the lower drop surface and interface for coarse and medium resolutions from the adaptive two-dimensional level-set simulations. The coalescence time is delayed by increasing local resolution.

5. Conclusions

The evolution of single droplets impacting on liquid/liquid interfaces was investigated experimentally using flow visualization and PIV. Two viscosity ratios (drop to ambient fluid), λ, of 0.14 and 0.33 were studied. Upon impact, the drop deformed the interface significantly before rebounding upward and eventually settling to a 'rest' position on top of a thin film. The vorticity initially present within the drop dissipated fairly rapidly due to drop/interface interaction as well as shearing of the trailing wake on the upper drop surface.

Equivalent axisymmetric and two-dimensional flows were simulated numerically using interface capturing phase-field and level-set methods respectively. The former uses a uniform mesh while the latter uses adaptive mesh refinement. Prior to impact, the phase-field method captures quantitatively the features seen in the experiment. However, resolving the near contact region using a uniform mesh is problematic due to the computational expense involved. Thus near the impact time, the lubrication forces are not resolved by the uniform mesh simulation and coalescence occurs prematurely. The adaptive simulations show significant improvement over the non-adaptive simulations in that increased local resolution in the near contact region better resolves the lubrication flow. Future work involves the development of adaptive axisymmetric and three-dimensional mesh refinement algorithms for the Navier-Stokes equations together with coupled level-set/volume-of-fluid methods that will enable accurate mass-conserving simulations to be performed.

Acknowledgments

This work was supported by the Engineering Research Program of the Office of Basic Energy Sciences at the U.S. Department of Energy (Grant DE-FG02-98ER14869). The first author was supported by a Doctoral Dissertation Fellowship from the University of Minnesota Graduate School and a scholarship for the Science University of Malaysia.

References

Christensen, K.T., Soloff, S.M., 2000. PIV Sleuth: integrated particle image velocimetry (PIV) interrogation/validation software. Technical Report 943, Dept. of Theoretical and Applied Mech., University of Illinois at Urbana Champaign.

Mohamed-Kassim, Z., Longmire, E.K. 2003. Drop impact on a liquid/liquid interface. Phys. Fluids, 15, 3263-3272.

Kim J.S., Kang K. and Lowengrub J.S. 2004. Conservative multigrid methods for Cahn-Hilliard fluids. J. Comp. Phys., 193, 511-543.

Zheng X., Cristini V., Lowengrub J.S. and Anderson A. 2004. An algorithm for adaptive remeshing of 2D and 3D domains: Application to the level-set method. J. Comp. Phys. In review.

Lowengrub J.S. and Truskinovsky L. 1998. Quasi-incompressible Cahn-Hilliard fluids and topological transitions. R. Soc. Lond. Proc. Ser. A Math. Phys. Eng. Sci., 454, 2617.

Mohamed-Kassim, Z., Longmire, E.K. 2004. Drop coalescence through a liquid/liquid interface. Phys. Fluids, in press.

Yang X., James A.J., Lowengrub J.S., Zheng X. and Cristini V. 2004. An adaptive coupled level-set /volume of fluid method. In preparation.